scifAI: Explainable machine learning for profiling the immunological synapse and functional characterization of therapeutic antibodies

Sayedali Shetab Boushehri[1,2,3,4*], Katharina Essig[5,*], Nikolaos-Kosmas Chlis[5], Sylvia Herter[6], Marina Bacac[6], Fabian J Theis[2,3], Elke Glasmacher[7,+], Carsten Marr[1,2,+], Fabian Schmich[4,+]

[1] Institute of AI for Health, Helmholtz Munich, Germany
[2] Institute of Computational Health, Helmholtz Munich, Germany
[3] Technical University of Munich, Department of Mathematics, Munich, Germany
[4] Data Science, Pharmaceutical Research and Early Development Informatics (pREDi), Roche Innovation Center Munich, Germany
[5] Large Molecule Research (LMR), Roche Pharmaceutical Research and Early Development (pRED), Roche Innovation Center Munich, Germany
[6] Discovery Oncology, Roche Pharmaceutical Research and Early Development (pRED), Roche Innovation Zurich, Switzerland
[7] RED (Research and Early Development), Roche Diagnostics Solutions, Roche Innovation Center Munich, Germany

*joint first
+co-corresponding

Abstract:

Therapeutic antibodies are widely used to treat severe diseases. Most of them alter immune cells and act within the immunological synapse; an essential cell-to-cell interaction to direct the humoral immune response. Although many antibody designs are generated and evaluated, a high-throughput tool for systematic antibody characterization and prediction of function is lacking. Here, we introduce the first comprehensive open-source framework, scifAI (single-cell imaging flow cytometry AI), for preprocessing, feature engineering and explainable, predictive machine learning on imaging flow cytometry (IFC) data. Additionally, we generate the largest publicly available IFC data set of the human immunological synapse containing over 2.8 million images. Using scifAI, we analyze class frequency- and morphological changes under different immune stimulation. T cell cytokine production across multiple donors and therapeutic antibodies is quantitatively predicted *in vitro,* linking morphological features with function and demonstrating the potential to significantly impact antibody design. scifAI is universally applicable to IFC data, and, given its modular architecture, straightforward to incorporate into existing workflows and analysis pipelines, e.g. for rapid antibody screening and functional characterization.

Keywords: immunological synapse, mechanistic insight, therapeutic antibodies, imaging flow cytometry, IFC, functional characterization, explainable, machine learning, AI, feature extraction, prediction, classification, computer vision, deep learning, python, framework

Introduction

The formation of an immunological synapse is the first event of the adaptive immune reaction induced by the interaction of a T cell with its corresponding antigen-presenting cell (APC). This rapidly formed cell-cell interface is initiated by the recognition of peptide-loaded MHC complexes by the T cell receptor (TCR). It involves the rearrangement of actin filaments of the cytoskeleton and the recruitment of signaling, co-stimulatory, co-inhibitory, and adhesion molecules to the nascent synapse [1,2]. This process is crucial to trigger and fine-tune T cell responses and ensure intact immune reactions. Dysfunctional immunological synapse formation has been observed in several immune-related disorders [3–8] and has thus been considered a potential target to stimulate or inhibit immune responses by modulating its assembly or function [9–11]. For instance, various therapeutic antibodies were developed that alter immunological synapse formation to treat cancer and autoimmune diseases [12–15]. Although significant progress in developing immunological synapse targeting agents has been achieved in the last years [9], there is still need to refine the compounds further, especially to improve their efficacy. It has been identified that antibody size and format [16,17], the dose, as well as target expression [18] can be critical parameters for immunological synapse formation and its effect on T cell function.

However, so far no study has provided a tool to systematically quantify and characterize the morphology of the immunological synapse, investigate its correlation to T cell response, or identify properties predictive for the efficacy of antibodies *in vitro*. As a consequence, only a literature-guided set of fluorescent stainings relevant for investigating the immunological synapse is set in an otherwise untargeted approach, allowing the exploration of a broad range of possible characteristics. The key technology for high-throughput data acquisition for this purpose is imaging flow cytometry (IFC), combining the benefits of traditional flow cytometry with deep, multi-channel imaging on the single-cell level. IFC has recently been successfully applied to visualize and quantify the immunological synapse of primary human T:APC cell conjugates [19–21], however, none of these studies investigated the formation of the immunological synapse in the context of T cell function.

Recent studies have demonstrated the potential of machine learning algorithms for a more robust and accurate analysis of high-throughput imaging data, an approach that has been demonstrated to overcome limitations of conventional gating strategies [22–24]. Leveraging machine learning for IFC data analysis has also enabled the identification of morphological patterns in the cell, a combined analysis of RNA and protein data, and the implementation of predictive models [22–26]. While limited open-source software implementations designed for IFC data analysis are available [26,27], they either rely on additional third-party software adding complexity in the analysis pipeline, or they focus on prediction performance only and lack explainability.

Here, we present scifAI, a machine learning framework for the efficient and explainable analysis of high-throughput imaging data based on a modular open-source implementation. We also publish the largest publicly available multi-channel IFC data set with over 2.8 million images of

primary human T-B cell conjugates from multiple donors, and demonstrate how scifAI can be used to detect patterns and build predictive models. We showcase the potential of our framework for (i) the prediction of immunologically relevant cell class frequencies, (ii) the systematic morphological profiling of the immunological synapse, (iii) the investigation of inter donor and inter and intra-experiment variability, as well as (iv) the characterization of the mode of action of therapeutic antibodies and (v) the prediction of their functionality *in vitro.* Combining high-throughput imaging of the immunological synapse using IFC with rigorous data preprocessing and machine learning enables researchers in pharma to screen for novel antibody candidates and improved evaluation of lead molecules in terms of functionality, mode-of-action insights and antibody characteristics such as affinity, avidity and format.

Results

Comprehensive multi-channel imaging flow cytometry data set of the immunological synapse

Using high-throughput IFC we generated a comprehensive data set for the systematic analysis of the immunological synapse of T-B conjugates (Fig. 1a and Supplementary Fig. 1a). Human memory $CD4^+$ T cells, isolated from peripheral blood of different donors, were co-cultured with superantigen (*Staphylococcus aureus* enterotoxin A, SEA)-pulsed EBV-transformed lymphoblastoid B cells (B-LCL) expressing high levels of the co-stimulatory molecules CD86 and CD80 or left untreated (Supplementary Fig. 1b-c and Supplementary Fig. 2a-b) . P-CD3ζ (Y142) as a readout of early T cell activation, the highest titrated concentration of SEA (100 ng/mL), and a time point of 45 min was chosen to investigate functional immune synapses (Supplementary Fig. 1 d-e). In total, we screened nine donors in four independent experiments (Supplementary Fig. 1a) and acquired 1,182,782 images (±SEA, Supplementary Fig. 1b). The designed multi-channel panel consisted of brightfield (BF), F-actin (cytoskeleton), MHCII, CD3, and P-CD3ζ (TCR signaling) allowed to capture a wide range of biologically motivated, potentially relevant characteristics of the immunological synapse (Fig. 1a). Dead, deformed, unfocused or cropped cells were removed using a multi-step pipeline (Methods). Additionally, a set of 5221 images from seven randomly selected donors was labeled by an expert immunologist (K.E.) into nine classes organized in two levels. (Fig. 1b and Supplementary Fig. 2e). The first level represented the number of existing cells in the image: singlets (n=1), doublets (n=2), and multiplets (n>2). The second level characterizes the type of the cells, their interactions to each other and the presence of TCR signaling. The singlets are composed of “single B-LCL”, “single T cell w/o signaling” and “single T cell w/ signaling” classes. The doublets include the “T cell w/ small B-LCL”, “B-LCL and T cell in one layer”, “synapse w/o signaling”, “synapse w/ signaling”, and “no cell-cell interaction” classes. The class “multi-synapse”, contains more than two cells and at least one B-LCL and T cell. Even though the ‘T cell w/ small B-LCL’ and ‘no cell-cell interaction’ classes were artifacts of the experiments, they were annotated to enhance the predictive power of classification models and subsequently filtered out and not used in further analyses (Methods).

scifAI: An explainable AI python framework for the analysis of multi-channel imaging flow cytometry data

As the foundation for all further analysis, we developed the single-cell imaging flow cytometry AI (scifAI) framework. The open-source framework was developed in python, leveraging functionality from state-of-the-art modules, such as scikit-learn, SciPy, NumPy and pandas (Methods), allowing for smooth integration and extension of existing analysis pipelines. Universally applicable for single-cell brightfield or fluorescent imaging projects, the framework provides functionality for import and preprocessing of input data, several feature engineering pipelines including the implementation of a set of biologically motivated features and autoencoder-generated features (Methods), as well as methodology for efficient and meaningful feature selection. Moreover, the framework implements several machine learning and deep learning models for training supervised image classification models, e.g. for the prediction of cell configurations such as the immunological synapse. Following the principle of multi-instance learning, the framework also implements functionality to regress a set of selected images, against a downstream continuous readout such as cytokine production. Extensive documentation, as well as how to reproduce the analysis in the form of Jupyter notebooks is provided online at https://github.com/marrlab/scifAI/ and https://github.com/marrlab/scifAI-notebooks.

scifAI enables high-throughput profiling of the immunological synapse

In order to characterize the immunological synapse in an unbiased fashion, we first designed and computed a series of biologically motivated, interpretable features using the scifAI framework. These features were based on morphology, intensity, co-localization, texture and synaptic features extracted from the 5-panel stained images and their corresponding masks (Methods and Supplementary Fig. 3a-b). Synaptic features were implemented based on the ratio of the signal intensity of each fluorescent channel in the synaptic area to the whole cell. Leveraging the large amount of unlabeled data, we also implemented a multi-channel convolutional autoencoder to learn a second set of data-driven features from the images in an unsupervised fashion [24]. The autoencoder was designed to encode the images to a 128-dimensional abstract feature space by reconstructing the input images (Methods).

Subsequently, scifAI was used to compose a supervised machine learning pipeline for the classification of the 5221 annotated images across the nine immunologically relevant cell classes. We trained and benchmarked a series of supervised machine learning models for the prediction of all nine classes using both the interpretable feature space as well as the abstract autoencoder features across all donors and experimental conditions. The models included an XGBoost classifier on the interpretable features and a multi-class logistic regression (LR) on the interpretable and data-driven features. To pre-select the features and reduce the dimensionality, we implemented a feature pre-selection pipeline using an ensemble of different methods (Methods and Supplementary Fig. 4a-b). We also trained a number of convolutional neural network (CNN) architectures such as Resnet18, ResNet34, DeseNet121 and DeepFlow which had previously been shown to be successful in classification tasks on imaging flow cytometry data [22,24,28]. The CNN architectures intrinsically learned a feature representation based on the

input images and their corresponding labels. All models were trained on a stratified subset, comprising 2923 (70%) annotated images. In order to benchmark the classification model and feature space combinations, we compared macro F1 scores on the remainder of images as the hold-out test set comprising 1567 (30%) annotated images (Methods). The XGBoost model using the interpretable feature set performed best (F1-macro=0.92±0.01, mean ± std 5-fold cross-validation with 10 repetition) among all the classifiers. It was followed by convolutional neural networks ResNet34 (0.91±0.01), ResNet18 (0.90±0.01), and DeepFlow (0.90±0.02). They were followed by multi-class logistic regression using the interpretable feature set (0.90±0.02), and logistic regression using the data-driven feature set (0.79±0.02). Based on the performance and explainability, the XGBoost model was selected as the final classifier for label expansion to the full dataset (Fig. 1c). Investigation of the model's confusion matrix on the hold-out set revealed that misclassifications occurred mostly within the cell classes' signaling property , whereas all other classes showed good overall concordance (Supplementary Fig. 4c). After training the XGBoost classifier, we also explored which underlying features drive the class prediction, ranking features by their respective Gini-index (Fig. 1E). The most predictive features were based on colocalization of CD3 & MHCII, colocalization of MHCII & P-CD3ζ, texture of MHCII and CD3, and intensity of P-CD3ζ. Based on the features and the definition of classes, one could speculate that the classifier uses (i) the texture of CD3 and MHCII to detect the existence of T and B-LCL cells in the image, (ii) the colocalization of CD3 & MHCII to detect the different doublets types and (iii) the intensity of P-CD3ζ and colocalization of MHCII & P-CD3ζ to detect whether there is a signaling T cell in the image (Fig. 1d).

A subset of annotated data and available IFC channels suffices for a high classification performance

Following the identification of the final model, we investigated how many annotated samples were necessary to reach a reasonable classification performance. We repeatedly trained the model on stratified subsets of the training data and evaluated the F1-macro on the test set. The results showed that by using 1500 images (45% of the training data), we could achieve 90% of F1-macro on the test set (Supplementary Fig. 5a). Next, we explored which channels were sufficient for reaching high performance. We kept the BF channel and used all possible combinations of the fluorescent channels to train the model. We found that the channels BF, MHCII and P-CD3ζ sufficed to reach an F1-macro similar to using all the channels (Supplementary Fig. 5b).

Characterizing the impact of therapeutic antibodies on synapse formation

We next used scifAI to investigate effects of therapeutic antibodies on the formation of the immunological synapse and to better characterize their morphological profiles. This analysis included the investigation of potential class frequency changes and feature differences. We chose two antibodies, one activator and one inhibitor of immune responses. The activating T cell bi-specific (TCB) antibody was designed to target CD3 and CD19, a co-receptor of B cells [29] (Fig. 2c). The inhibitory antibody, Teplizumab, is described to only bind to CD3 (Fig. 2a) and has been shown to dampen T cell responses [30,31]. For each antibody an appropriate control (Ctrl-TCB and isotype) was run within the same experiment and donor. Since Teplizumab

required an existing immune response for subsequent inhibition, we used SEA to first stimulate the T cells (Fig. 2c). The same setup was also used for the isotype control. Six donors across two experiments for CD19-TCB and seven donors across three experiments for Teplizumab were measured (Fig. 2b,d and Supplementary Fig. 2c-d). To determine class frequency changes between the antibody and its control, the previous XGBoost classifier (Fig. 1c,d) was used to predict the class for all images based on the interpretable features (Methods). To ensure that the previously trained XGBoost model was transferable from ±SEA to the antibody experiments, an expert (K.E.) annotated a randomly selected subset of 396 images for CD19-TCB and 227 images for Teplizumab. A high concordance between ground truth annotations and XGBoost predictions on the new experiments (macro F1-score=0.86 for TCB and 0.85 for the Teplizumab) confirmed that the trained model generalizes across experiments and can thus be utilized for further analyses (Supplementary Fig. 6a). For a compact representation of class frequency changes, we computed log2-fold changes between the antibodies and their controls. In a second step, we focused on the feature differences of synapses under antibody stimulation and selected all the images predicted as 'synapses w/ signaling' for each donor and compared interpretable features from only fluorescent channels including texture, synaptic features, morphology, intensity and co-localization between antibodies and their controls. We avoided using the BF channel as its intensity is difficult to interpret and its morphological characteristics can be captured also by other fluorescent channels (Methods).

CD19-TCB increases the formation of stable immune synapses

Stimulation of the immune response by CD19-TCB led to a significant increase of doublets and multiplets frequencies. The 'synapse w/ signaling' class showed thereby the highest increase (median log_2(CD19-TCB/Ctrl-TCB)=2.7, n=6 donors, p=0.036) followed by 'multi-synapse' (median=2.03, p=0.036), 'B-LCL & T cell in one layer' (median=1.99,p=0.036), and 'synapse w/o signaling' class (median=0.59,p=0.036). For the singlets, the overall trend was a decrease in class frequency of 'single B-LCL' (median=-0.21, p=0.036) and `single T cell w/o signaling` (median=-0.77, p=0.036) (Fig. 2e).

Next, we investigated the feature differences in synapses induced by the CD19-TCB (Methods), comparing the 210 interpretable features from all fluorescent channels. We found 210 significantly increased and 163 significantly decreased features out of 210*6=1260 possibilities from combination of features and donors (Fig. 3a). All donors exhibited mostly similar responses towards the stimulation with CD19-TCB. On average 27±4 features were significantly decreased and 33±7 features were significantly increased per donor (dashed lines bottom Fig. 3a). From these features, we were able to find a number of features with similar changes within at least 4 out of 6 donors (Fig. 3a and Supplementary Table 1). We also observed an increase in 'mean intensity of P-CD3ζ' with higher enrichment within the synaptic area (Fig. 3b-c and Supplementary Table 1). In addition, we also detected a stronger enrichment of F-actin and MHCII towards the synapse (Fig. 3d-g). Taken together, the observed increase in doublet and multiplet frequencies as well as a stronger enrichment of F-actin and MHCII in the synaptic area indicated an enhanced formation of tight immunological synapses, translating into an efficient

TCR signaling. These observations are in line with the mode of action that is already described in general for TCBs, promoting a stable interaction between tumor cells and T cells [32–34].

Teplizumab alters synapse formation and TCR signaling

In contrast to the CD19-TCB, treatment with Teplizumab reduced the frequency of doublets and multiplets significantly (Fig. 2f). The highest decrease was observed for the 'synapse w/ signaling' class (median log_2(Teplizumab/Isotype)=-0.75, n=7, p=0.022), followed by 'multiplets' (median=-0.69, p=0.036), and 'synapse w/o signaling' (median=-0.57, p=0.022). Accordingly, 'single T cell w/ signaling' (median=0.70, p=0.022) and 'single B-LCL' (median=0.09, p=0.022) were increased significantly as compared to the isotype. Surprisingly, the T cell w/o signaling' class frequency was significantly decreased (median=-0.30, p=0.022), probably due to the significant increase of 'single T cell w/ signaling' (Fig. 2f).

We next investigated feature differences in synapses induced by Teplizumab in seven donors. From 'synapses w/ signaling' images we extracted 132 features based on F-actin, MHCII and P-CD3ζ and their co-localizations. CD3 features could not be included for the analysis because the binding of Teplizumab and the anti-CD3 staining antibody interfere, therefore an anti-CD4 staining antibody was used to identify T cells. We found 131 significantly increased and 169 significantly decreased features out of 132*7=924 possibilities (Fig. 3h and Supplementary Table 2). In particular, Teplizumab, on average, led to 25±8 significantly decreased features and 19±17 significantly increased features per donor (dashed lines bottom Fig. 3h). Donor 6 showed the least number of changes with five significantly increased features. In contrast, donor 4 yielded the highest number of increased features with 50 features, indicating a fair amount of inter donor-variability. We found a set of features which were significantly increased or decreased for at least 5 out 7 donors (Fig. 3i,k). We observed a decrease in the mean intensity of F-actin whereas donor 2 and 4 indicated a significant increase (Fig. 3i,j). This opposite reaction of the two donors could be also detected for other F-actin related features (Supplementary Table 2). Besides the changes in F-actin features, we also detected a significant reduction of P-CD3ζ intensity within the synapse and observed a stronger clustering of TCR signaling around the whole T cell (Fig. 3k,l). In conclusion, we gained new insights into the immunosuppressive mode of action of Teplizumab as we observed a reduction in the number of synapses as well as changes in the F-actin reorganization and P-CD3ζ signaling towards the synapse.

Morphological profiles of the immunological synapse predict functionality of therapeutic antibodies in vitro

Next, the capabilities of scifAI in predicting the functionality of antibodies by analyzing T cell cytokine production were explored. We included an additional antibody in our analysis, the CD20-TCB. CD20-TCB is a therapeutic antibody with the same format similar to CD19-TCB but varying target moiety [32]. Given the richness of interpretable features, we investigated whether it is possible to forecast downstream T cell responses as measured by GrzmB for the TCBs. While the IFC measurement was taken after 45 minutes, GrzmB was measured after 24 hours, respectively, using conventional FACS for each donor and condition to address the effects of the

antibodies in later time points (Fig. 4b). In line with the differences in target expression, the CD20-TCB (20.23±6.32, n=4) showed the highest expression of GrzmB, followed by the CD19-TCB (12.58±3.04) and Ctrl-TCB (1.16±0.51) (Fig. 4b and Supplementary Fig. 6b). A similar pattern was also detected for killing of two tumor cell lines with different expression levels of CD19 and CD20 (Supplementary Fig. 6c-d).

Since there is a one-to-many relationship between FACS cytokine measurements and IFC images, where each cytokine measurement corresponds to an IFC cell population consisting of 54,708 images on average, an aggregation pipeline based on the interpretable features was implemented (Methods). For each donor and condition, first images predicted as synapses were selected and their previously extracted features were aggregated using the 5th, 50th, and 95th percentile. This aggregation ensured that every feature's extrema and average expression were captured (Fig. 4c and Methods). Next, it was attempted to predict the cytokines for an unseen antibody. Due to the low number of samples, a linear model with Lasso Lars penalization was used (Methods). The cross validation was performed on CD19-TCB and CD20-TCB, while the No Ab and Ctrl-TCB were kept in the training set. The prediction performance reached a Spearman correlation of 0.38. While we could observe subtle differences between the predictions and the ground truth, the model correctly identified the separation between CD20-TCB and CD19-TCB. Furthermore, the model suggested that the 'standard deviation of MHCII (95th perc.) [intensity]' and 'eccentricity of F-actin (95th perc.) [morphology]' as the most important features.

Discussion

In the present work we established scifAI, a pipeline based on two innovative technologies, imaging flow cytometry and explainable machine learning to understand the mode of action and predict the functionality of therapeutic antibodies *in vitro*. We analyzed morphological profiles of the immunological synapse to better characterize the mode of action of therapeutic antibodies early after the initiation of an immune response and to apply it to forecast downstream T cell responses.

We generated the largest publicly available imaging flow cytometry data using human primary immune cells from nine donors in four independent experiments that were treated with various therapeutic antibodies to study synapse formation. This is in contrast to previous works that did not take into account inter-experiments effects on synapse formation [21,35]. To detect and study immunological synapses, we implemented an interpretable feature extraction and machine learning framework in python by only using well-maintained python modules. This choice guarantees performance, scalability, reproducibility and facilitates the deployment into existing workflows, which differs from previous works that use a combination of CellProfiler, R and python for each stage of the analysis [27,36,37]. The combination of using interpretable features and explainable machine learning enabled us to identify various relevant classes, such as immunological synapses, with state-of-the-art accuracy. It also allowed us to investigate the morphological profiles of the immunological synapse in an unbiased way as well as the characterization of the mode of action of antibodies in a biologically relevant context. This methodology is thus a substantial contribution to the field which is otherwise primarily focused on performance over interpretability by using ResNet CNN architecture as the backbone [26,38].

To demonstrate the capabilities of the scifAI framework we investigated the effects of two therapeutic antibodies on the immunological synapse, the CD19-TCB and Teplizumab, which are both binding CD3 and have been described to activate and suppress T cell responses, respectively [29–31]. We found that the CD19-TCB forms more stable immune synapses as indicated by a stronger enrichment of MHCII and F-actin within the synapse that was paralleled by a higher intensity of P-CD3ζ. The formation of stable T cell-tumor cell synapses has already been reported for other TCBs like the CEA- and CD20-TCB [32,33]. In contrast to the CD19-TCB, treatment of Teplizumab yielded a decrease in synapse formation and prevented F-actin reorganization as well as localization of P-CD3ζ towards the synapse. These observations gave new insights into the immunosuppressive mode of action of Teplizumab that has rarely been investigated *in vitro* so far [30,31]. One could speculate that steric hindrance by Teplizumab prevented T cell-APC interactions leading to less stable synapses and reduced cytokine production. It has been shown that antibody size and format can have a substantial impact on synapse formation [16,17]. Another hypothesis could be that binding of Teplizumab induced strong TCR internalization that led to diminished SEA-mediated TCR-MHCII crosslinking and thus inhibited T cell activation. The reduced P-CD3ζ intensity in the synaptic area and the observed unpolarized distribution of P-CD3ζ signal around the whole T cell could also indicate altered TCR signaling that might be translated into a reduced T cell effector function. High numbers of peripheral P-CD3ζ microclusters have been already reported for self-reactive T cells with altered

synapse formation and aberrant T cell responses [6]. Interestingly, scifAI identified features within the synapse class revealing inter donor-variability upon stimulation with the different antibodies. However, we were not able to correlate the variability of those features to a different functionality *in vitro* because the differences in the T cell responses between donors were just minor. Patient material from ongoing clinical trials could help to further elaborate if these synapse features could be used to predict clinical response. In that case, scifAI could enable us to rapidly screen for responders *in vitro* and potentially pre-select suitable patients for clinical trials. Taken together, by applying scifAI we were not only able to thoroughly investigate the mode of action of therapeutic antibodies by identifying significant features, but also to gain more insights into inter donor-variability that might potentially translate into different functional outcomes *in vivo*.

The immunological synapse has previously been studied using high-content cell imaging on human cell lines and primary cells with an artificial APC system that utilized plate-bound ICAM-1 and stimulatory antibodies [37]. Although German et al. convincingly demonstrated the capabilities of their pipeline by profiling the immunological synapse, they did not investigate whether they can use these profiles in predicting drug effectiveness [37]. In other studies, the potential of synapse formation was also investigated for CAR T cell therapy, where investigators used the mean intensity of stainings such as F-actin and P-CD3ζ per cell, clustering of tumor antigen and polarization of perforin-containing granules as a measure of synapse formation quality. These features varied between different CAR T cells and correlated with their effectiveness *in vitro* and *in vivo* as well as with clinical outcomes [39,40]. In our work, we improved this by incorporating 296 biologically motivated features such as texture, intensity statistics and synaptic related features.

This work is the first in using interpretable features of the immunological synapse to predict the effectiveness of therapeutic antibodies on T cell cytokine production. These features allowed us to predict the functional outcome of an unseen antibody and to pinpoint the driving factors required for the prediction. For the TCBs we found intensity of MHCII and morphology of F-actin as the most prominent features in predicting cytokine readouts. The ability to predict unseen antibodies could potentially enable the investigation of various antibody formats to better understand mechanistically how different formats can impact T cell responses and help to guide format selection.

scifAI is an end-to-end data acquisition and analysis framework which can be adjusted to investigate various hypotheses and to develop diverse applications based on imaging flow cytometry data. For instance, while in this study memory $CD4^+$ T cells were analyzed as they are poised to show faster immune responses and a higher synapse propensity compared to naive T cells [49], imaging and analysis of $CD8^+$ T cells, as the main players in cytotoxicity, could further elaborate how synapse features correlate with killing efficiency of therapeutic antibodies against tumor cells. scifAI can also be utilized in the design of IFC experiments, optimizing the number and type of stainings, as well as the total number of images per donor to be acquired. In Pharma R&D, scifAI has the great potential to improve the quality and the speed of antibody development, for example giving new insights towards the mode of action of particular candidate molecules, or to predict *in vitro* efficacy in high-throughput. AI assisted identification of lead molecules and better prioritization in terms of epitope, affinity, avidity and antibody format

can have a huge impact on the decision making process. Above that, we can foresee that scifAI can even help to identify responders among patient populations and predict their clinical outcomes. In a nutshell, IFAI could provide substantial benefit by assisting the investigation of the mode of action and the functionality of newly generated antibody candidates.

Acknowledgements

The authors thank Ronan Le Gleut from the Core Facility Statistical Consulting at Helmholtz Munich for the statistical support. We thank Florian Limani from the Roche Innovation Center Zurich for running the killing assays. We acknowledge the Core Facility Flow Cytometry at the Biomedical Center, Ludwig-Maxmilians-Universität München, for providing equipment, services and expertise. Finally, we thank all members of the CD19-TCB and CD20-TCB team as well as colleagues from Large Molecule Research (LMR) and Cancer Immunotherapy, Oncology at Roche Pharmaceutical Research and Early Development (pRED) for their valuable input and scientific discussion.

Competing interests

The authors declare no competing interests.

Software and data availability

The scifAI code and instructional notebooks on how to run the code and built analysis pipelines can be found under

- https://github.com/marrlab/scifAI/
- https://github.com/marrlab/scifAI-notebooks

The data can be accessed here: https://doi.org/10.5061/dryad.ht76hdrk7 (it is still under revision by data Dryad and the link will be functional soon).

Author contributions

KE designed and performed the experiments. SSB wrote the analysis code and created the figures. SSB and KE wrote the manuscript with input from EG, CM and FS. EG, CM and FS conceived the study. NK and FT helped with the manuscript narrative, analysis ideas and editing. SH and MB provided scientific input, designed experiments and supported the writing of the manuscript. All the authors have read and approved the manuscript.

Funding

SSB has received funding by F. Hoffmann-la Roche LTD (No grant number is applicable) and supported by the Helmholtz Association under the joint research school ‘Munich School for Data Science - MUDS’.

Materials & Methods

Cell line culture

EBV-transformed B-lymphoblastoid cell line (B-LCL) from donor 333 was obtained from Astarte Biologics (# 1038-3161JN16) and cells were cultivated in RPMI-1640 medium (PAN-Biotech; cat # P04-17500) with 10% FBS (Anprotec; cat # AC-SM-0014Hi) and 2 mM L-glutamine (PAN-Biotech; cat# P04-80100). Z138 (MCL, gift from University of Leicester) and Nalm-6 (ALL, DSMZ ACC 128) tumor cells were cultivated in RPMI1640 containing 10% FBS and 1% Glutamax (Invitrogen/Gibco # 35050-038).

Immune synapse formation and imaging flow cytometry

To analyze immune synapses, human memory $CD4^+$ T cells were isolated from PBMCs of nine healthy human donors using a negative selection EasySep Enrichment kit from STEMCELL Technologies (cat #19157). Live/dead staining of T and B-LCL cells was separately performed using the fixable viability dye eF780 for 15 min at RT (eBioscience; cat # 65-0865-14). Cells were then re-suspended in RPMI-1640 medium supplemented with 10% FBS (Anprotec; cat # AC-SM-0014Hi), 5% Penicillin-Streptomycin (Gibco; cat # 15140-122) and 2 mM L-glutamine (PAN-Biotech; cat # P04-80100). Afterwards B-LCL cells were transferred into a well of a 96-well round bottom plate (300.000 cells per well) and were pre-incubated with the superantigen Staphylococcal enterotoxin A (SEA) (Sigma-Aldrich; cat # S9399) for 15 min at 37°C or left untreated. Human $CD4^+$ T_{mem} were added to the afore-prepared B-LCL cells (250.000 cells per well) to generate a final ratio of 4:3 (B-LCL:T_{mem}) and subsequently the appropriate in-house made compounds (10 µg/mL of Isotype Ctrl or Teplizumab and 1 µg/mL (5 nM) of Ctrl-TCB, CD19-TCB or CD20-TCB) were added to the B-LCL-T_{mem} cell co-culture. To strengthen the conjugate formation between B-LCL and T cells they were centrifuged at 300xg for 30 sec and then directly transferred to a 37°C incubator for 45 min. Thereafter, the medium in each well was carefully aspirated with a pipette and cells were immediately fixed for 12 min at RT followed by permeabilization using the Foxp3/Transcription factor staining buffer set from eBioscience (cat # 00-5523-00). Intracellular staining was performed in permeabilization buffer containing fluorescently-labeled antibodies for 40 min at 4°C: CD3-BV421 (clone UCHT1, Biolegend; cat # 300433), HLA-DR-PE-Cy7 (clone L243, Biolegend; cat # 307616), Phalloidin AF594 (ThermoFisher; cat # A12381) and P-CD3ζ Y142-AF647 (K25-407.69, BD cat # 558489). After washing, cells were suspended in FACS buffer (PBS supplemented with 2% FBS) and acquired on an Amnis ImageStream^X Mark II Imaging Flow Cytometer (Luminex) equipped with five lasers (405, 488, 561, 592 and 640 nm). On average, around 55,000 images were collected per sample at 60x magnification on a low speed setting. IDEAS software (version 6.2.187.0, EMD Millipore) was used for data analysis and labeling of cells. To identify immune synapses using the IDEAS software the gating strategy in Supplementary Fig 1a was implemented. Cells were first gated on in-focus $live^+$ $CD3^+$ $MHCII^+$ cells. Within this population images that show single $CD3^+$ T cells and single $MHCII^+$ B-LCL cells were selected using the area and aspect ratio feature. Next, to exclude non-interacting cells the CD3 intensity within a self-created synapse

mask was determined. The synapse mask was defined as a combination of the morphology CD3 and MHCII mask with a dilation of 3. Only synapses that showed a CD3 signal in the mask were gated. Finally, T+B-LCL cells in one layer were excluded by using the height and area feature of the brightfield (BF) and single T-B-LCL synapses were analyzed.

Intracellular staining of cytokines using conventional flow cytometry

For intracellular cytokine staining cells were first treated with GolgiPlug (BD Biosciences; cat # 555029) and GolgiStop (BD Biosciences; cat #554724) for at least 2-4 h before being stained. After incubation live/dead staining was performed using the fixable viability dye eF780 for 20 min at 4°C (eBioscience; cat # 65-0865-14). Cells were then fixed and permeabilized using the Foxp3/Transcription factor staining buffer set from eBioscience (cat # 00-5523-00) as described for the synapse formation assay. Intracellular staining was performed in permeabilization buffer containing fluorescently-labeled antibodies for 30 min at 4°C: TNFα-APC (clone MAb11, BD Biosciences; cat # 554514), IFN-γ-PE (clone B27, BD Biosciences; cat # 554701) and Granzyme B-PE-Cy7 (clone QA16A02, Biolegend; cat # 372214). Finally, cells were suspended in FACS buffer (PBS supplemented with 2% FBS and 1 mM EDTA) and acquired on a FACS Celesta from BD Biosciences.

Tumor Cell Lysis Assays (in vitro)

B cell-depleted PBMCs derived from blood of healthy donors were prepared using standard density-gradient isolation followed by B cell depletion with CD20 Microbeads (Miltenyi; cat # 130-091-104). B cell-depleted PBMCs were then incubated with the tumor targets (Z-138 or Nalm-6) at a ratio of 5:1 for 24 h in the presence or absence of CD20-TCB or CD19-TCB. Tumor cell lysis was calculated based on LDH release (LDH Cytotoxicity Detection Kit from Roche Applied Science) and normalized to spontaneous release (PBMCs + targets without treatment = 0 % tumor cell lysis) and maximal release (lysis of tumor targets with Triton X-100 = 100 % lysis).

Quantification of CD20 and CD19 expression

CD19 and CD20 expression on B-LCL cells were determined using the Quantum™ Alexa Fluor® 647 MESF Kit from Bangs Laboratories (cat # 647) according to the manufacturer's instructions using an anti-human CD20-AF647 (Biolegend # 302318) or and anti-human CD19-AF647 (Biolegend # 302220) antibody as well as the corresponding isotype controls (muIgG1 (Biolegend # 400130) and muIgG2b (Biolegend # 400330). For the quantification of CD19 and CD20 molecules on the tumor target cell lines Nalm-6 and Z-138 the QiFi Kit from Dako (cat # K0078) was performed according to the manufacturer's instructions by using an anti-human CD20 purified (BD # 555621) or and anti-human CD19 purified (BD # 555410) antibody as well as the corresponding isotype controls (muIgG1 (BD # 554121) and muIgG2b (BD # 557351).

Preparation of the imaging dataset for analysis

We in total recorded 2,899,575 imaging flow cytometry images. The dataset consists of nine distinct donors across four independent experiments. Donor 1 and Donor 2 were used twice (Supplementary Fig. 2a). Different conditions were measured which included -SEA (total images=625,001), +SEA (557,781), Ctrl-TCB (330,000), CD19-TCB (324,020), CD20-TCB (254,398), Isotype (405,000), and Teplizumab (403,375). The images contained brightfield (BF), F-actin, MHCII, CD3, P-CD3ζ, and live-dead stainings. The live-dead staining is only used to filter out the dead cells. For each experiment, the images were compensated using a compensation matrix derived from stained single cells. After the compensation, the raw images (16-bit) and their corresponding channel-wise segmentation masks were exported from the IDEAS software and saved in an HDF5 format. To enable parallelization, each image and its corresponding mask were saved separately.

Interpretable feature engineering from images

We extracted a set of 296 biologically motivated features to study the immunological synapse. These features included morphology, intensity, co-localization, texture and synaptic related values (see Supplementary Fig. 3). The morphology features were calculated based on the segmentation mask from each channel. The features included ‘area’, ‘bounding box area’, ‘convex area’, ‘eccentricity’, ‘equivalent diameter’, ‘Euler number’, ‘extent’, ‘maximum Feret diameter’, ‘minimum Feret diameter’, ‘filled area’, ‘length of major axis’, ‘length of minor axis’, ‘Hu moments’, ‘orientation’, ‘perimeter’, ‘Crofton perimeter’, ‘solidity’, ‘weighted Hu moments’. All the morphology features are extracted using `scikit-image` library [41]. For the intensity features, first the cells were segmented using their corresponding mask. The intensity features included ‘min’ ,‘sum’, ‘mean’, ‘standard deviation’, ‘skewness’, ‘kurtosis’, ‘max’ and ‘Shanon entropy’. In addition, the percentile of intensity values including ‘10th percentile’, ‘20th percentile’, …, ‘90th percentile’ were calculated. All of the intensity features were calculated based on `NumPy` [42] and `SciPy` [43] functionality. For co-localization features, we implemented ‘dice distance’ and ‘Jaccard distance’ to calculate the masks overlap between two channels using the `SciPy` [43] library. In addition, we calculated the ‘correlation distance’ [43], ‘Euclidean distance’ [43], ‘Manders overlap coefficient’ [44], ‘intensity correlation quotient’ [44], ‘structural similaity’ [41] and ‘Hausdorff distance’ [41]. For texture features, we used Gray Level Co-occurrence Matrix (GLCM) features [45] including ‘contrast’, ‘dissimilarity’, ‘homogeneity’, ‘ASM’, ‘energy’ and ‘correlation’. The synapse related features were defined as ‘enrichment of Ch (mean)’= $mean(intensity\ of\ Ch\ in\ synapse)/mean(intensity\ of\ Ch)$, ‘enrichment of Ch (sum)’= $sum(intensity\ of\ Ch\ in\ synapse)/sum(intensity\ of\ Ch)$, and ‘enrichment of Ch (max)’= $max(intensity\ of\ Ch\ in\ synapse)/mean(intensity\ of\ Ch)$ [35]. Finally, we implemented ‘background mean’ and ‘gradient RMS’ for quality control of images. All these features were implemented using `NumPy(version=1.18.5)`, `Pandas (1.1.5)`, `SciPy (1.8.0)`, `scikit-image (0.19.2)`, and `scikit-learn(1.0.2)` [46].

Autoencoder feature extraction

To leverage the large amount of unlabeled data, we implemented and trained a multichannel

autoencoder [24]. This autoencoder included a separate encoder for each channel. The encoders were designed to map each channel to a 32 dimensional vector. The concatenation of these vectores led to a 5*32 dimensional space. Then these features were mapped to a 256 dimensional feature vector. A decoder on top of the concatenated vectors was implemented for reconstructing the original image. 'L2 norm' was used as the reconstruction loss. The augmentations used for training the autoencoder included random rotation, random scaling, random flipping, random gaussian noise.

Feature pre-selection

Considering that the number of features was large, we implemented a feature pre-selection pipeline to select the most relevant features. We followed the work of Haq et al. [47] (see Supplementary Fig. 4a). First, the Pearson correlation between the features was measured. If at least two features were highly correlated (|corr|>0.95), then only one of them was kept (at random), and the rest were eliminated. In the next step, six different methods were used to rank the features. These methods included mutual information, linear support vector machine, logistic regression with L1 regularization, logistic regression with L2 regularization, random forest, and XGBoost. The *top-k* (hyper-parameter to be selected) features from each method were selected, and their union was used. After this reduction, the Spearman correlation matrix between the features was calculated, and spectral clustering was performed on the correlations. Then, *m* clusters were created, and one feature at random per cluster was selected. The last step was performed to account for multicollinearity between the features.

Classification

There are three main approaches which are used for training a supervised learning algorithm in this work, feature based approach and deep learning.

Classical supervised learning models

We used two different algorithms for training machine learning models. We used a boosting method called XGBoost [48] which uses an ensemble of trees on the data (n_trees=100). The second model was a logistic regression. The advantage of using these models was that they provide explainability after the training.

Convolutional neural networks

For training supervised deep learning models, we used well-known architectures in the field of computer vision including ResNet18, Resnet34, ResNet50, ResNet152, DeseNet121 and DeepFlow [22,24,28]. All of the models were pre-trained on ImageNet. Considering the models are designed for three channels input, we had to remove the first convolutional layer with three input channels to six input channels. In addition, the classification layer also needed to be adjusted to have nine classes. However, the rest of the networks were untouched with their predefined ImageNet weights. We used multi-class cross entropy loss for training. The learning rate (lr) was set to 0.001, with adaptive strategy of reducing on plateau of 10 epochs. The augmentations used for training the autoencoder included random rotation, random scaling, random flipping,

random gaussian noise.

Classification feature importance

As mentioned, a feature pre-selection filtering was used to reduce the number of features and then an XGBoost classifier was trained on the annotated data. While the XGBoost can provide feature importance using Gini-index, these importances can be biased due to different reasons such as correlation between the pre-selected features, number of features, the pre-selection process, outliers , etc. To account for this, we splitted the training data randomly to 5-folds (stratified) and trained the XGBoost classifier five times, each time using 4 out of the 5 folds. We repeated this process 100 times, leading to 500 different models. In each training, we used a random number of pre-selected features (top-k) between 30 to 200 features. Eventually, for every feature a series of Gini-indices were obtained. The median Gini-index for each feature was used to rank the features.

Classification staining importance

To determine which staining contributes the most to the predictions, we used recursive channel elimination. In every run, we always kept BF as it is stain-free. Then train the 'interpretable features + XGBoost' based on the features of the selected channels (see Supplementary Fig. 5b).

Class frequency analysis

For each donor, first we used the trained XGBoost classifier to predict the classes for every image. Then we excluded images using this data cleaning protocol:

1. Filtering out images including dead cells (using Live-Dead staining) with 'mean Live-Dead intensity' >='mean Live-Dead intensity (90th perc.)'
2. Filtering out dead cells (using Live-Dead staining) with 'mean Live-Dead intensity' > 'mean Live-Dead intensity (90th perc.)'
3. Filtering out unfocused images with these conditions 'Gradient RMS BF' > 'Gradient RMS BF (2nd perc.)' and 'Gradient RMS BF' < 'Gradient RMS BF (90th perc.)'
4. Filtering out images based with high entropy using the XGBoost predictions (entropy> 1.0). The entropy was calculated using the SciPy package. This step is done to omit images that the classifier is the most uncertain in terms of prediction.
5. Filtering out images predicted as 'B-LCL' with 'mean intensity of MHCII' < 'mean intensity of MHCII (5th perc.)'. This step guarantees that the images predicted 'B-LCL' contain a minimum MHCII intensity
6. Filtering out images predicted as 'B-LCL' with 'area of MHCII' < 'area of MHCII (10th perc.)'. This step guarantees that the images predicted 'B-LCL' contain a cell with appropriate size and reduces artifacts.
7. Filtering out images predicted as 'T cell' with 'mean intensity of CD3'< 'mean intensity of CD3 (1st perc.)'. This step guarantees that the images predicted 'T cell' contain a minimum CD3 intensity.

8. Filtering out images predicted as 'B-LCL and T cell in one layer' with 'area of MHCII' < 'area of MHCII (20th perc.)'. This step is performed to omit 'B-LCL and T cell in one layer' with small 'B-LCL's.
9. Filtering out images based on the isolation forest outlier detection. We used n_estimators=100, max_samples='auto', contamination='auto', and max_features=20 as the main parameters. For reducing the run time, we only used top 30 features based on Gini-index from the XGBoost training.
10. Filtering out images based on Uniform Manifold Approximation and Projection (UMAP). First we transformed all images to 2D dimensional space using UMAP. The features were standardized using the mean and std of each feature. For reducing the run time, we only used top 30 features based on Gini-index from the XGBoost training. Then a DBSCAN algorithm was run with eps=0.09 and min_samples=5. The resulted clustered were filtered out if (#images in cluster)/(#total images) < 0.0001.

All these steps are done based on scikit-learn implementations. All parameters were set using the default value of scikit-learn unless stated otherwise. After the data cleaning, the frequency of each class was calculated with 'F_C=(#images predicted as C)/(#total images)' for each condition per donor. To deal with the compositional nature of the data, we used log_2(F_C_antibody/F_C_control) to compare the frequency fold-changes. This transformation has the advantage that the frequencies do not sum to a constant value. After calculating the log_2 fold-changes, we used the Wilcoxon-rank-sum test for analyzing the effects of antibodies on class frequencies. Wilcoxon-rank-sum tests whether two samples are likely to derive from the same population. To account for multiple testing, we used Benjamini-Hochberg correction for +SEA/-SEA, CD19-TCB/Control TCB and Teplizumab/isotype respectively. Because the experiments were performed independently, we only corrected each of these comparisons separately.

Feature difference analysis

We analyzed the effect of perturbation with CD19-TCB, and Teplizumab on signaling synapses. First, we selected the images predicted as 'synapse w/ signaling'. We removed brightfield (BF) features as the intensity of BF does not contain biological meaning. Also, the morphological features of BF were already captured based on F-actin masks. Therefore this information was redundant. This feature reduction was also necessary as it reduces the number of tests and increases the chance of finding meaningful p-values after correction for multiple testing. This procedure yielded 210 features for comparison for SEA and TCB based on F-actin, MHCII, CD3, and P-CD3ζ. For Teplizumab, we had to reduce the features even more. This reduction was necessary because of the usage of CD4 in recording images for Teplizumab instead of CD3. Therefore, a meaningful comparison between Teplizumab and its control based on CD3 was not feasible. Thus we analyzed 132 features extracted from F-actin, MHCII, and P-CD3ζ.

After the feature selection, we compared the features using the Mann-Whitney U test for each condition and its control. To understand the direction of change, we used the difference in median of features for each condition and its control. To account for multiple testing, we used the Benjamini-Hochberg procedure with α=0.05. As the conditions were independent, we

corrected the p-values for each condition and its control separately.

GrzmB prediction and feature ranking

To predict GrzmB, we only used images predicted as ‘synapse w/o signaling’ and ‘synapse w/ signaling’ for each condition. This choice was done as it is assumed that the synapses will lead to cytokine production. Considering that for each donor and condition we had thousands of images, we used an aggregation pipeline to create a feature vector corresponding to each donor and condition. To reduce the number of features, we only used the consistent feature changes for the CD19-TCB (Fig. 3). For each donor and condition, we aggregated the features using 5th, 50th and 95th percentile to capture the extremes and average of every feature.

After deriving the aggregated features, we used a one-donor-leave-out cross validation to train a linear regression model with LassoLars. The most important features were based on the magnitude of the coefficients.

Visualizations

For visualizing the conjugates and biological context, we used www.BioRender.com. For the plots and images, we used `matplotlib (version=3.3.2)` and `seaborn (0.11.2)` in Python. Finally, Inkscape was used for creating the figures.

References

1. Huppa, J. B. & Davis, M. M. T-cell-antigen recognition and the immunological synapse. *Nat Rev Immunol* **3**, 973–983 (2003).
2. Dustin, M. L. The Immunological Synapse. *Cancer Immunol Res* **2**, 1023–1033 (2014).
3. C.J., K., A.J., B., P.K., D. & J., O. The role of the immunological synapse formed by cytotoxic lymphocytes in immunodeficiency and anti-tumor immunity. *Crit Rev Immunol* **35**, 325–347 (2015).
4. Kallikourdis, M., Viola, A. & Benvenuti, F. Human Immunodeficiencies Related to Defective APC/T Cell Interaction. *Front Immunol* **6**, 433 (2015).
5. R., D., Laura *et al.* Imbalance of immunological synapse-kinapse states reflects tumor escape to immunity in glioblastoma. *Jci Insight* **3**, e120757 (2018).
6. Schubert, D. A. et al. Self-reactive human CD4 T cell clones form unusual immunological synapses. *J Exp Medicine* **209**, 335–352 (2012).
7. Ronan Calvez, et al. The Wiskott-Aldrich syndrome protein permits assembly of a focused immunological synapse enabling sustained T-cell receptor signaling. *Haematologica* **96**, 1415–1423 (2011).
8. G., R., Alan et al. Chronic lymphocytic leukemia T cells show impaired immunological synapse formation that can be reversed with an immunomodulating drug. *J Clin Invest* **118**, 2427–2437 (2008).
9. Francesca, F. & Baldari, C. T. The immunological synapse as a pharmacological target. *Pharmacol Res* **134**, 118–133 (2018).
10. Tai, Y., Wang, Q., Korner, H., Zhang, L. & Wei, W. Molecular Mechanisms of T Cells Activation by Dendritic Cells in Autoimmune Diseases. *Front Pharmacol* **9**, 642 (2018).
11. M., S.-T., Scott, Yun-jeong, S., M., S., Richard & J., O., John. Steward-Tharp et al., Ann. NY. Acad. Sci 2010, New insights into T cell biology and T-cell directed therapy for autoimmunity, inflammation, and immunosuppression.pdf. *Ann Ny Acad Sci* **1183**, 123–148 (2010).
12. Wetzel, S. A., McKeithan, T. W. & Parker, D. C. Live-Cell Dynamics and the Role of Costimulation in Immunological Synapse Formation. *J Immunol* **169**, 6092–6101 (2002).
13. Cremasco, F. et al. Cross-linking of T cell to B cell lymphoma by the T cell bispecific antibody CD20-TCB induces IFNγ/CXCL10-dependent peripheral T cell recruitment in humanized murine model. *Plos One* **16**, e0241091 (2021).
14. Amita, J. et al. An Overview of the Pharmacokinetics and Pharmacodynamics of Efalizumab: A Monoclonal Antibody Approved for Use in Psoriasis. *J Clin Pharmacol* **46**, 10–20 (2006).
15. Lee, J. Y. et al. Structural basis of checkpoint blockade by monoclonal antibodies in cancer immunotherapy. *Nat Commun* **7**, 133**5**4 (2016).
16. Dickopf, S., Georges, G. J. & Brinkmann, U. Format and geometries matter: Structure-based design defines the functionality of bispecific antibodies. *Comput Struct Biotechnology J* **18**, 1221–1227 (2020).
17. Cartwright, A. N. R., Griggs, J. & Davis, D. M. The immune synapse clears and excludes molecules above a size threshold. Nat Commun 5, 5479 (2014).
18. Vyver, A. J. V. D. et al. Predicting Tumor Killing and T-Cell Activation by T-Cell Bispecific Antibodies as a Function of Target Expression: Combining In Vitro Experiments with Systems Modeling. *Mol Cancer Ther* **20**, 357–366 (2021).

19. Wabnitz, G. H., Nessmann, A., Kirchgessner, H. & Samstag, Y. InFlow microscopy of human leukocytes: A tool for quantitative analysis of actin rearrangements in the immune synapse. *J Immunol Methods* **423**, 29–39 (2015).
20. Wabnitz, G. H. et al. L-plastin phosphorylation: A novel target for the immunosuppressive drug dexamethasone in primary human T cells. *Eur J Immunol* **41**, 3157–3169 (2011).
21. Ahmed, F., Friend, S., George, T. C., Barteneva, N. & Lieberman, J. Numbers matter: Quantitative and dynamic analysis of the formation of an immunological synapse using imaging flow cytometry. J Immunol Methods **347**, 79–86 (2009).
22. Lippeveld, M. et al. Classification of Human White Blood Cells Using Machine Learning for Stain-Free Imaging Flow Cytometry. *Cytom Part A* **97**, 308–319 (2020).
23. Eulenberg, P. et al. Reconstructing cell cycle and disease progression using deep learning. Nat Commun 8, 463 (2017).
24. Kranich, J. et al. In vivo identification of apoptotic and extracellular vesicle-bound live cells using image-based deep learning. *J Extracell Vesicles* **9**, 1792683 (2020).
25. Chlis, N.-K., Rausch, L., Brocker, T., Kranich, J. & Theis, F. J. Predicting single-cell gene expression profiles of imaging flow cytometry data with machine learning. *Nucleic Acids Res* **48**, gkaa926- (2020).
26. Doan, M. et al. Deepometry, a framework for applying supervised and weakly supervised deep learning to imaging cytometry. *Nat Protoc* **16**, 3572–3595 (2021).
27. Hennig, H. et al. An open-source solution for advanced imaging flow cytometry data analysis using machine learning. *Methods San Diego Calif* **112**, 201–210 (2017).
28. Eulenberg, P. et al. Reconstructing cell cycle and disease progression using deep learning. *Biorxiv* 081364 (2017) doi:10.1101/081364.
29. Leclercq, G. et al. JAK and mTOR inhibitors prevent cytokine release while retaining T cell bispecific antibody in vivo efficacy. *J Immunother Cancer* **10**, e003766 (2022).
30. Xu, D. et al. In Vitro Characterization of Five Humanized OKT3 Effector Function Variant Antibodies. *Cell Immunol* **200**, 16–26 (2000).
31. Herold, K. C. et al. Activation of human T cells by FcR nonbinding anti-CD3 mAb, hOKT3γ1(Ala-Ala). J Clin Invest **111**, 409–418 (2003).
32. Cremasco, F. et al. Cross-linking of T cell to B cell lymphoma by the T cell bispecific antibody CD20-TCB induces IFNγ/CXCL10-dependent peripheral T cell recruitment in humanized murine model. Plos One 16, e0241091 (2021).
33. Bacac, M. et al. A Novel Carcinoembryonic Antigen T-Cell Bispecific Antibody (CEA TCB) for the Treatment of Solid Tumors. *Clin Cancer Res* **22**, 3286–3297 (2016).
34. Marina, B. et al. Bacac et al., Clinc Cancer Res 2018, CD20-TCB with Obinutzumab pretreatment as next-generation treatment of hematologic malignancies .pdf. Clin Cancer Res **24**, 4785 (2018).
35. Wabnitz, G., Kirchgessner, H. & Samstag, Y. Qualitative and Quantitative Analysis of the Immune Synapse in the Human System Using Imaging Flow Cytometry. *J Vis Exp* (2019) doi:10.3791/55345.
36. Carpenter, A. E. et al. CellProfiler: image analysis software for identifying and quantifying cell phenotypes. *Genome Biol* **7**, R100–R100 (2006).
37. German, Y. et al. Morphological profiling of human T and NK lymphocytes by high-content cell imaging. *Cell Reports* **36**, 109318 (2021).

38. Perakis, A. et al. Contrastive Learning of Single-Cell Phenotypic Representations for Treatment Classification. *Arxiv* (2021) doi:10.1007/978-3-030-87589-3_58.
39. Naghizadeh, A. et al. In vitro machine learning-based CAR T immunological synapse quality measurements correlate with patient clinical outcomes. *Plos Comput Biol* **18**, e1009883 (2022).
40. Xiong, W. et al. Immunological Synapse Predicts Effectiveness of Chimeric Antigen Receptor Cells. *Mol Ther* **26**, 963–975 (2018).
41. Walt, S. van der et al. scikit-image: image processing in Python. *Peerj* **2**, e453 (2014).
42. Harris, C. R. et al. Array programming with NumPy. *Nature* **585**, 357–362 (2020).
43. Virtanen, P. et al. SciPy 1.0: fundamental algorithms for scientific computing in Python. *Nat Methods* **17**, 261–272 (2020).
44. Adler, J. & Parmryd, I. Quantifying colocalization by correlation: The Pearson correlation coefficient is superior to the Mander's overlap coefficient. Cytom Part A **77A**, 733–742 (2010).
45. Haralick, R. M., Shanmugam, K. & Dinstein, I. Textural Features for Image Classification. *Ieee Transactions Syst Man Cybern* **SMC-3**, 610–621 (1973).
46. Buitinck, L. et al. API design for machine learning software: experiences from the scikit-learn project. Arxiv (2013).
47. Haq, A. U., Zhang, D., Peng, H. & Rahman, S. U. Combining Multiple Feature-Ranking Techniques and Clustering of Variables for Feature Selection. *Ieee Access* **7**, 151482–151492 (2019).
48. Krishnapuram, B. et al. XGBoost. *Proc 22nd Acm Sigkdd Int Conf Knowl Discov Data Min* 785–794 (2016) doi:10.1145/2939672.2939785.

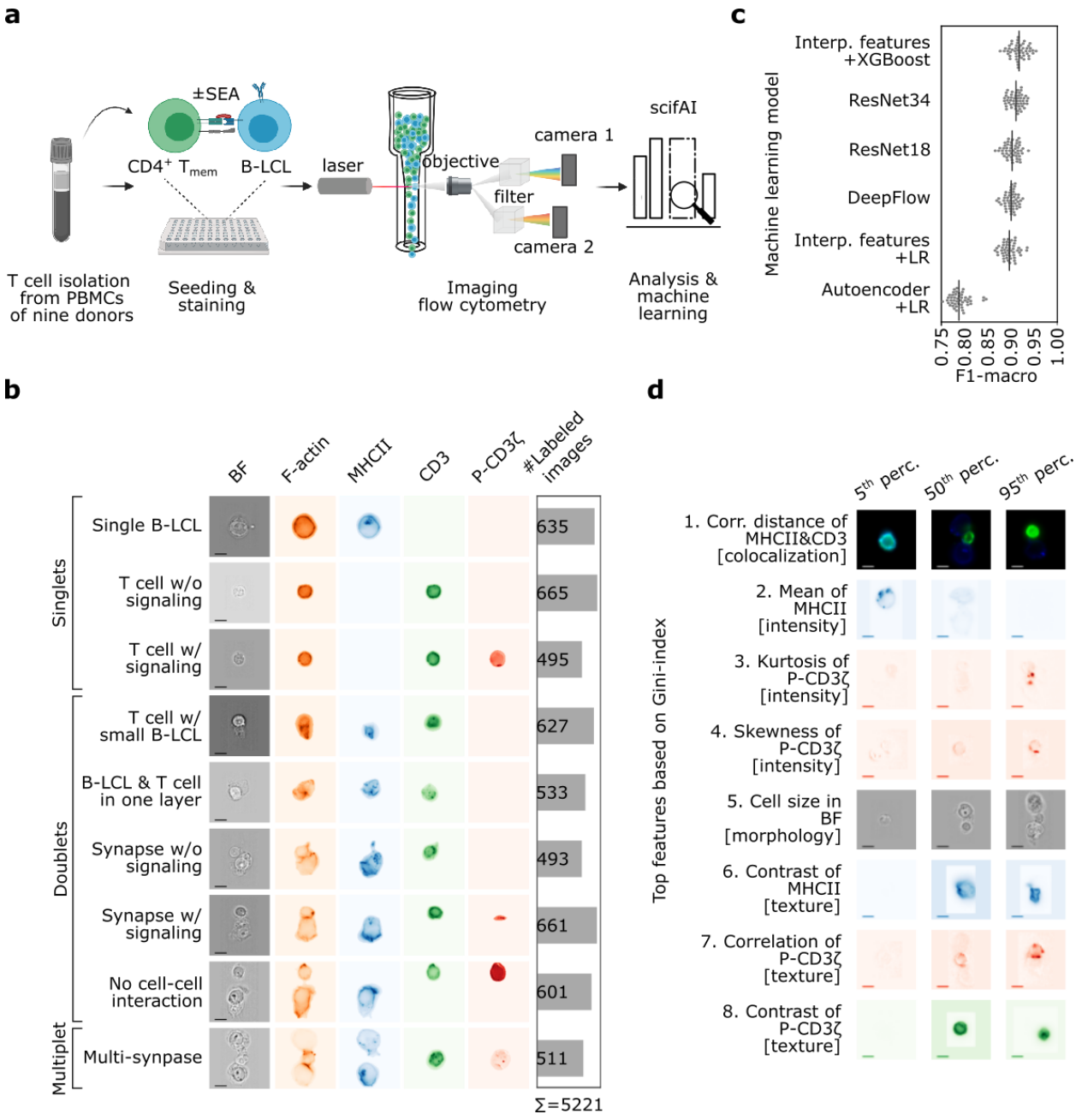

Figure 1: Explainable machine learning accurately predicts immunologically relevant cell classes from IFC data and identifies most informative image features.

a Schematic representation of the data generation and analysis pipeline. To systematically analyze the immunological synapse of T-B conjugates, 1,182,782 images were acquired with an imaging flow cytometer. Next, scifAI was used to extract morphological features, train machine learning models, profile immunological synapses and characterize the functionality of therapeutic antibodies.

b A subset of 5221 images was annotated by an expert into nine immunologically relevant classes that can be grouped into singlets (either B or T cells), doublets (with one B and one T cell), and multiplets (containing >2 cells). Cell images show brightfield (BF, scale bar = 2.4µm), F-actin (cytoskeleton), MHCII, CD3 and P-CD3ζ (a marker for TCR signaling).

c Six different approaches to train predictive machine learning models for the identification of the immunologically relevant classes were benchmarked, combining different classification algorithms and feature engineering strategies. These approaches included interpretable (interp.) features combined with explainable classifiers, an autoencoder to generate data-driven features, an explainable classifier, and three convolutional neural networks. Interpretable features combined with the XGBoost classifier resulted in the best trade-off between interpretability and classification performance.

d Top eight features for the detection of cell classes were ranked based on Gini-index. The features include colocalization, texture and intensity of MHCII, CD3 and P-CD3ζ. The exemplary images are taken from donor 7 in experiment IV (Supplementary Fig. 2) sampling from the 5th, 50th and 95th percentile of the distribution of each feature.

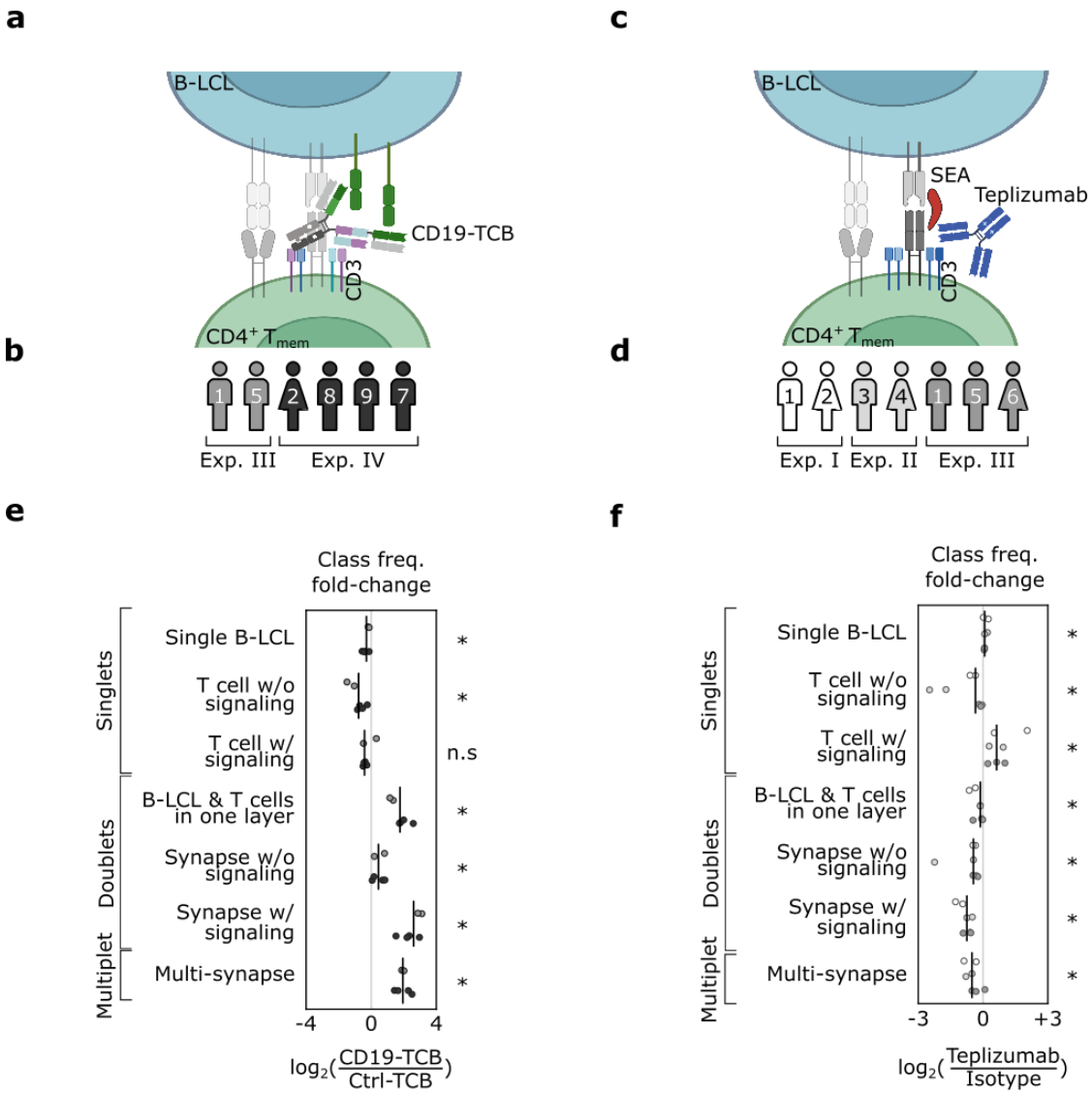

Figure 2. CD19-TCB and Teplizumab show significant changes in frequencies of synapses

a, c Schematic representation of the mode of action of CD19-TCB and Teplizumab.

b, d Donors and their respective experiments that were used for the class frequency analysis in Fig 3. e-f and feature difference analysis in Fig. 4.

e-f Class frequency differences depicted as log2 fold-changes between CD19-TCB or Teplizumab and their corresponding controls (Ctrl TCB & isotype). Each dot represents a donor color coded as in **b** or **d.** The vertical black line is the median across donors for each class.

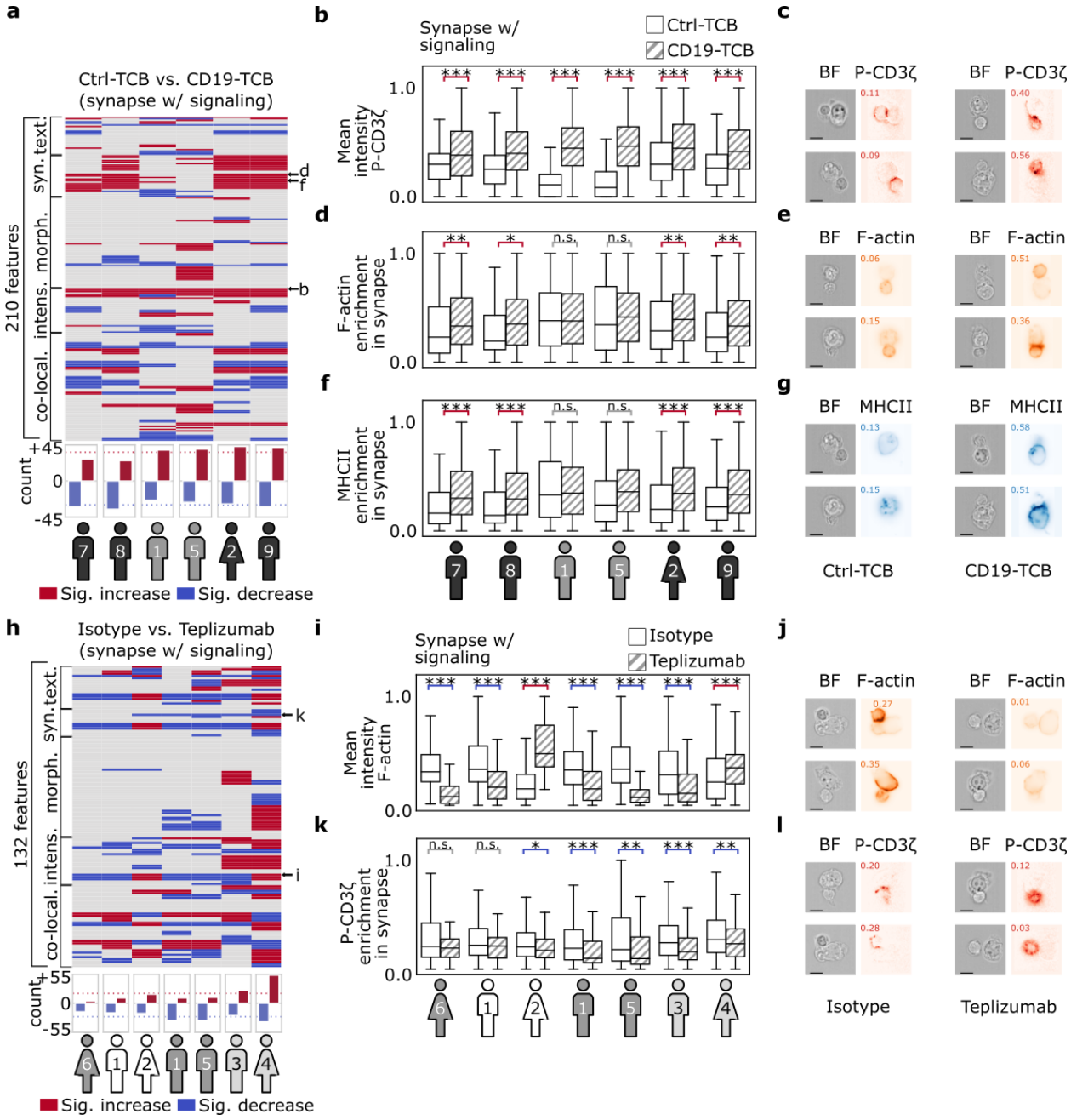

Figure 3. CD19-TCB and Teplizumab induce morphological changes on synapse formation including texture, intensity and synaptic features.

a Systematic comparison of 210 relevant features between CD19-TCB and Ctrl-TCB across images predicted as 'synapse w/ signaling' across six donors. Each line represents a feature and each column represents a donor. For each donor, the features which are significantly increased are depicted with red and the significantly decreased ones are depicted with blue. The donors are sorted based on the number of significantly changed features. The bottom bar plot shows the count of increased or decreased features per donor. Heatmap rows with arrows are shown in detail in **b**,**d** and **f**.

b, d, f Statistical and visual inter-donor comparison of three representative features between CD19-TCB and Ctrl-TCB. For visualization purposes, the features are mapped between zero and one for each donor separately.

c, e, g Visual representatives for all features were randomly sampled for both Ctrl-TCB and CD19-TCB from donor 9, and were found to be in concordance with the statistical results (scale bar = 2.4µm).

h Systematic comparison of 132 relevant features between Teplizumab and isotype across images predicted as 'synapse w/ signaling' among all six donors. The color code, barplot and sorting are the same as described in **a**.

i, k Statistical and visual inter-donor comparison of two representative features between Teplizumab and its isotype (also shown by three small arrows in **h**).

j, l Visual representatives for two features were randomly sampled for both isotype and Teplizumab from donor 3 and were found to be in concordance with the statistical results (scale bar = 2.4µm).

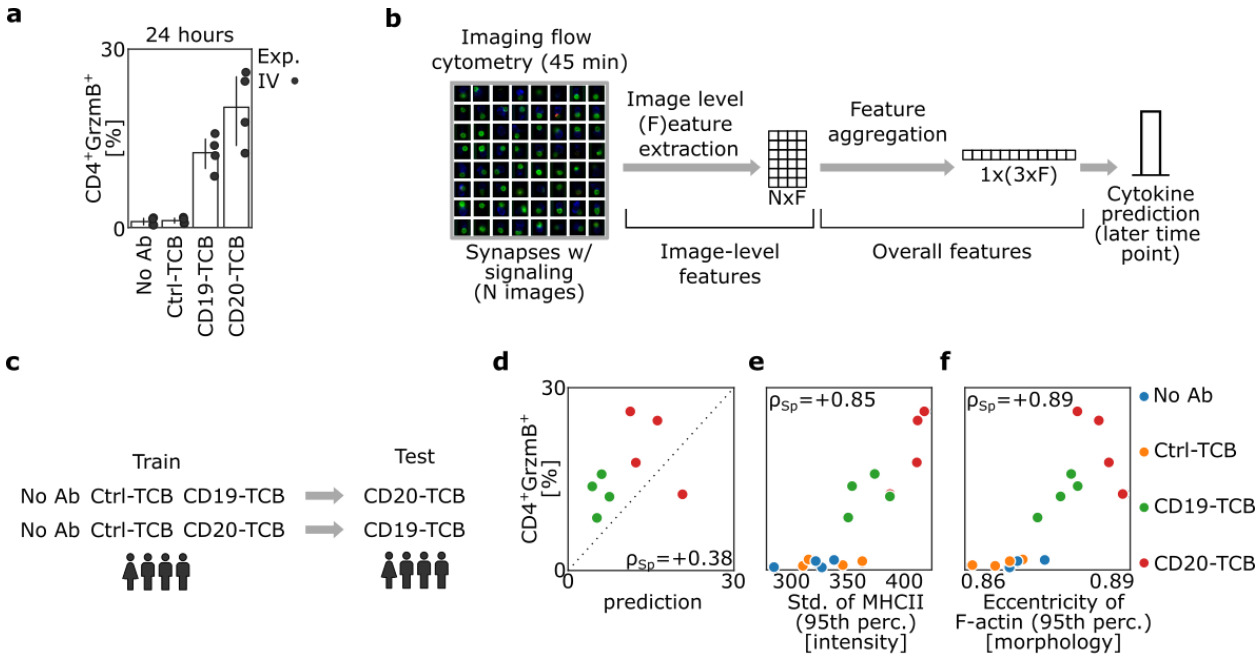

Figure 4. Morphological profiles of synapses are predictive of the functionality of antibodies in vitro.

a Frequencies of GrzmB$^+$ CD4$^+$ T cells measured by FACS after 24 hours. Corresponding to each imaging flow cytometry experiment, a separate FACS experiment was performed with the same batch to obtain the cytokine production values. Each dot represents a donor, color represents experiments.

b Data aggregation pipeline: For each donor and condition, images identified as synapses with and without signaling are selected (N = number of detected images). Then image-level features (F = number of relevant features) are extracted across all selected images. For each donor and condition, the features were aggregated using 5th, 50th and 95th percentile. This 620 dimensional aggregated feature reduces the cytokine prediction to a multivariate regression task.

c Analysis scheme: Cytokines are predicted for an unseen activator antibody by only using the control (No Ab and Ctrl-TCB) and another activator antibody. Data originates from one experiment with four donors.

d Scatterplot of the predictions versus ground truth values of GrzmB$^+$ CD4$^+$ frequencies. The dots are only based on the predictions from (c).

e,f Scatterplot of the features 'standard deviation of MHCII (95th percentile)' and 'eccentricity of F-actin (95th percentile)' versus the GrzmB$^+$ CD4$^+$ frequencies. These two features were selected based on the trained linear model in (d). Both features show high correlation with respect to GrzmB$^+$ CD4$^+$ frequencies.

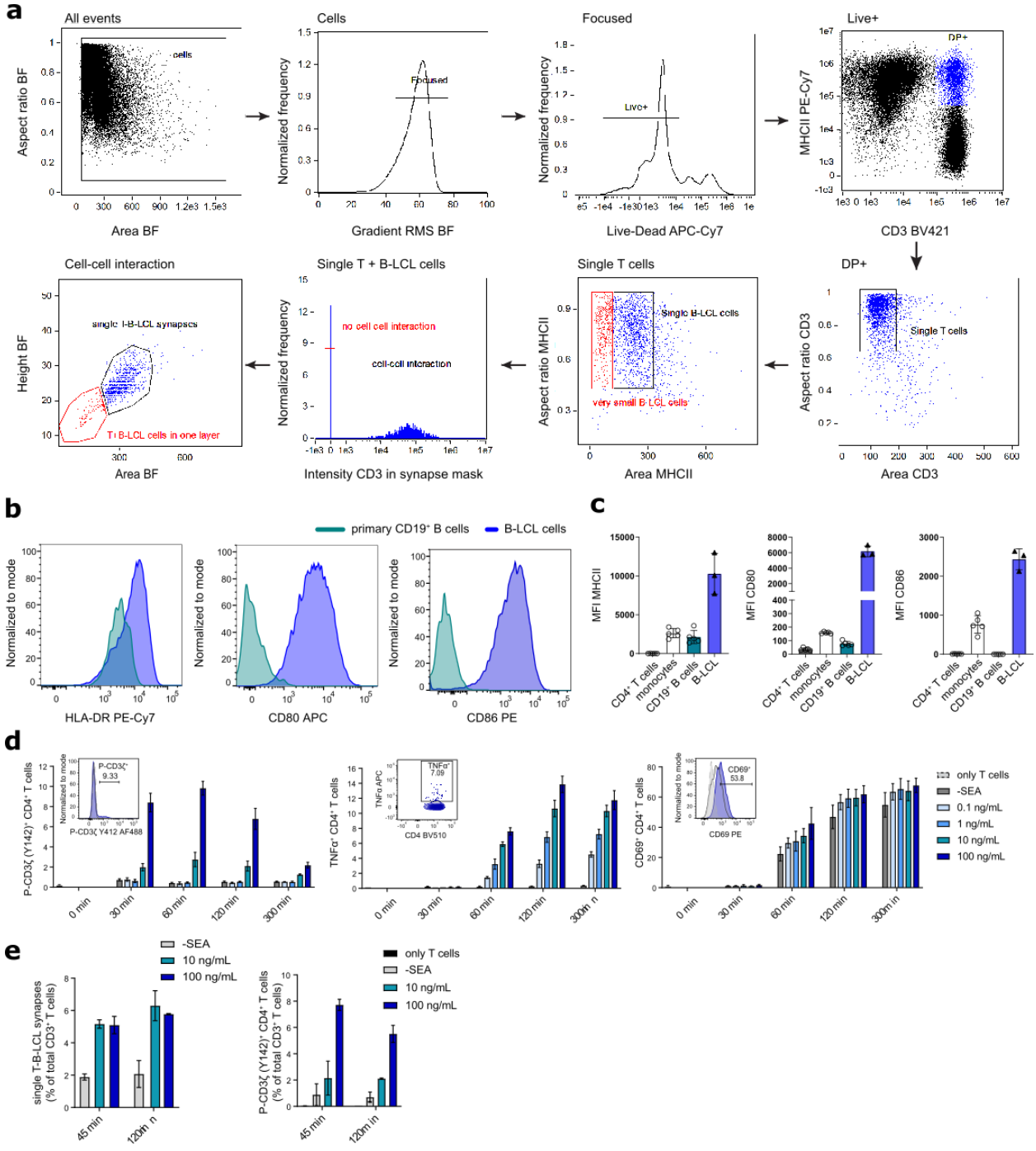

Supplementary Figure 1: Assay conditions to analyze immune responses between primary human CD4+ T cells and B-LCL cells using conventional and imaging flow cytometry

a Gating strategy to identify single interacting T-B-LCL synapses using the IDEAS software of the imaging flow cytometer.

b FACS histograms showing the surface-expression levels of MHCII (HLA-DR), CD80 and CD86 of primary CD19+ B cells from PBMCs and B-LCL cells.

c Quantification (MFI) of MHCII, CD80 and CD86 surface expression on primary CD4+ T cells, CD19+ B cells and monocytes from PBMCs and B-LCL cells. Data are from five donors in three independent experiments. The B-LCL cell line was analyzed in triplicates.

d Pre-testing of assay conditions using conventional FACS. Primary memory $CD4^+$ T cells isolated from PBMCs of healthy donors were stimulated with B-LCL cells in the presence of different concentrations of SEA (0.1-100 ng/mL) or left untreated (-SEA). Frequencies of P-CD3ζ^+, TNF-α^+ and $CD69^+$ $CD4^+$ T cells were determined at various time points. The small FACS histograms in the bar graphs show the expression levels of the three markers by comparing the highest concentration of SEA (100 ng/mL) with the untreated control (-SEA) after 60 min. The data shown represents one experiment using T cells from three different donors.
e Percentage of single T-B-LCL synapses and P-CD3ζ^+ $CD4^+$ T cells measured by imaging flow cytometry between two different SEA concentrations (10 and 100 ng/mL) after 45 and 120 min. Data represents two donors.

a

	Exp. I		Exp. II		Exp. III			Exp. IV			
Donor	1	2	3	4	1	5	6	2	7	8	9
Age [years]	>50	30-50	30-50	>50	>50	30-50	<30	30-50	30-50	30-50	>50

b

	Experimental condition	Name referred in text	Donors										
w/ & w/o SEA	B-LCL + CD4⁺ T cell	-SEA or No Ab	✓	✓	✓	✓	✓	✓	✓	✓	✓	✓	✓
	B-LCL + CD4⁺ T cell + SEA	+SEA	✓	✓	✓	✓	✓	✓	✓	✓	✓	✓	

c

control and activators	B-LCL + CD4⁺ T cell + Ctrl-TCB	Ctrl-TCB					✓	✓		✓	✓	✓	✓
	B-LCL + CD4⁺ T cell + CD19-TCB	CD19-TCB					✓	✓		✓	✓	✓	✓
	B-LCL + CD4⁺ T cell + CD20-TCB	CD20-TCB					✓	✓		✓	✓	✓	✓

d

control and inhibitors	B-LCL + CD4⁺ T cell + SEA + Isotype	Isotype	✓	✓	✓	✓	✓	✓	✓	✓			
	B-LCL + CD4⁺ T cell + SEA + Teplizumab	Teplizumab	✓	✓	✓	✓	✓	✓	✓	✓			

e

		Donors								
		1	1	2	3	5	7	8	9	
Singlets	Single B-LCL	127	125	74	68	101	51	41	48	635
	T cell w/o signaling	147	153	47	70	109	53	43	43	665
	T cell w/ signaling	64	124	64	67	42	47	41	46	495
Doublets	T cell w/ small B-LCL	80	182	41	72	109	55	44	44	627
	B-LCL & T cell in one layer	85	101	69	68	95	31	41	43	533
	Synapse w/o signaling	38	114	43	81	102	33	38	44	493
	Synapse w/ signaling	61	161	58	147	28	101	47	58	661
	No cell-cell interaction	86	120	75	80	75	87	32	64	601
Multiplet	Multi-synpase	45	164	14	66	74	52	79	47	511

Supplementary Figure 2. Donors and experiments information

a List of the donors, their age, gender and experiment numbers which are used in this study.

b List of experiments and donors with and without SEA.

c List of experiments and donors with TCBs and their control.

d List of experiments and donors with Teplizumab and isotype control

e Number of labeled by expert data per donor

a

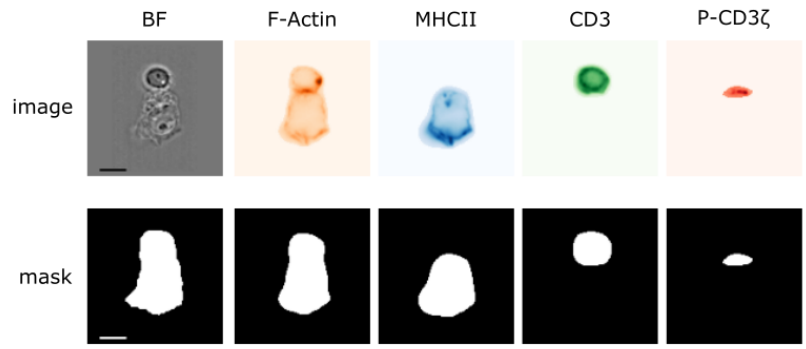

b

Morphology features
Input: image + mask

01. Cell area
02. Bounding box area
03. Convex area
04. Eccentricity
05. Equivalent diameter
06. Euler number
07. Extent
08. Feret diameter maximum
09. Filled area
10. Major axis length
11. Minor axis length
12. Hu moments
13. Orientation
14. Solidity
15. Weighted Hu moments

Synaptic features:
Input: image + mask

01. Enrichment of intensity in synaptic area (sum-based)
02. Enrichment of intensity in synaptic area (mean-based)
03. Enrichment of intensity in synaptic area (max-based)

Others:

01. Background mean
02. Gradient RMS

Intensity statistics:
Input: image + mask

01. Mean intensity
02. Standard deviation
03. Skewness
04. Kurtosis
05. Minimum intensity
06. Maximum intensity
07. Percentiles of intensity
08. Shannon entropy

Co-localization:
Input: two channels at a time

01. Correlation distance
02. Euclidean distance
03. Manders overlap coefficient
04. Structural similarity
05. Hausdorff distance

Texture features:
Input: image

01. Contrast
02. Dissimilarity
03. Homogeneity
04. ASM
05. Energy
06. Correlation

Supplementary Figure 3. scifAI interpretable feature list.

a Visual representation of each multi-channel image and corresponding masks. Masks were exported along with images from the IDEAS software

b List of all features implemented in scifAI. The morphology, intensity statistics, textures synaptic features are based on one channel. The colocalization features are based on two channels. scifAI automatically detects the existing channels and generates the specified features.

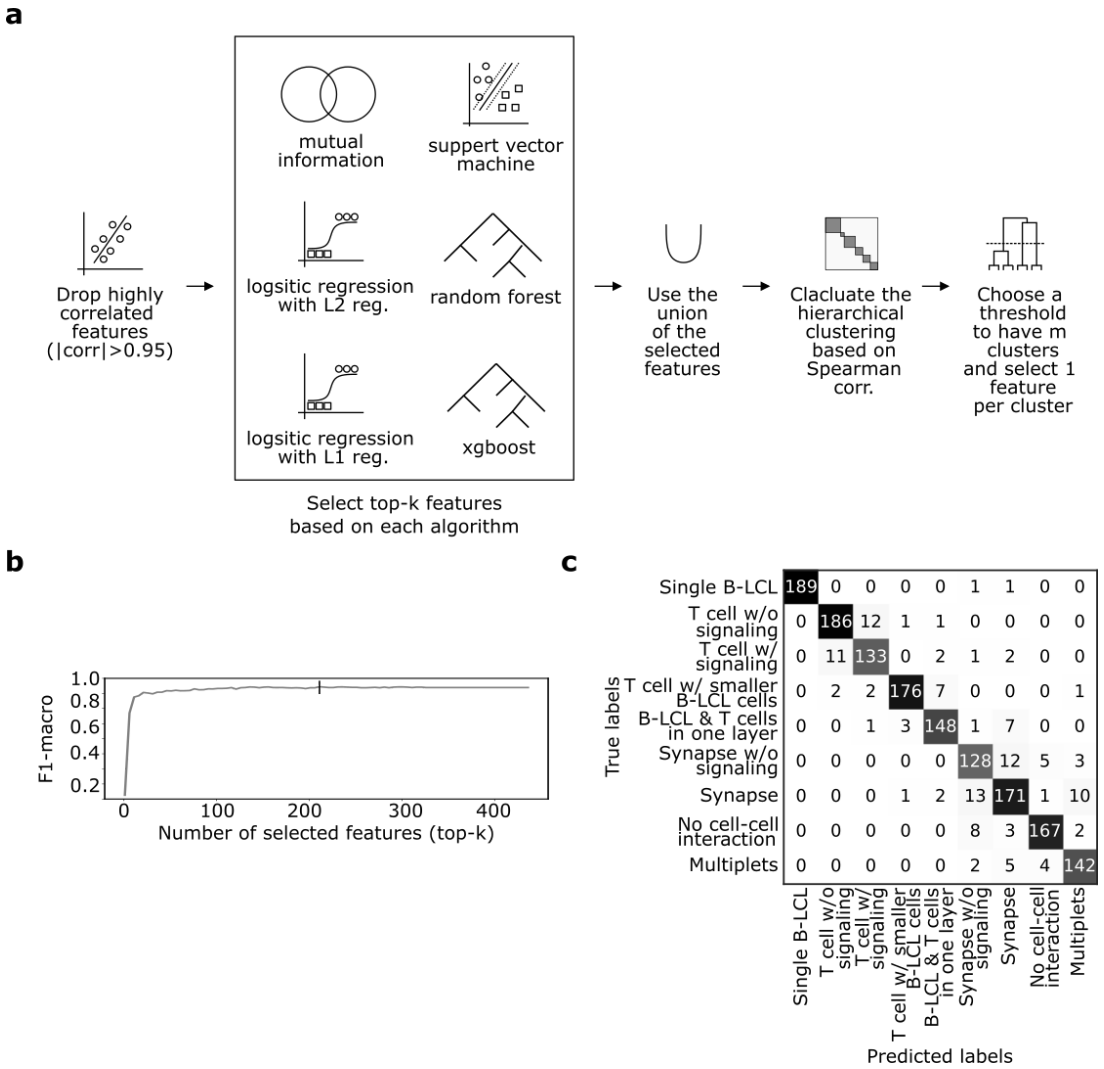

Supplementary Figure 4. Machine learning pipeline for classification.

a Feature pre-selection pipeline to reduce the dimensionality of the feature space and removing multicollinearity. First the highly correlated features are dropped. Then an ensemble of different classifiers is trained on the data, and their top-k features are selected. Finally, hierchical clustering is done on top of the union of the features to account for multicollinearity.

b The optimal number of selected features before passing the selected features to the XGBoost classifier. For obtaining the optimal top-k the data selection pipeline + XGboost was trained on stratified randomly selected 85% of the training set and tested on the rest 15%.

c Confusion matrix of the data selection pipeline (top-k = 211) + XGBoost, based on the predictions on the test set.

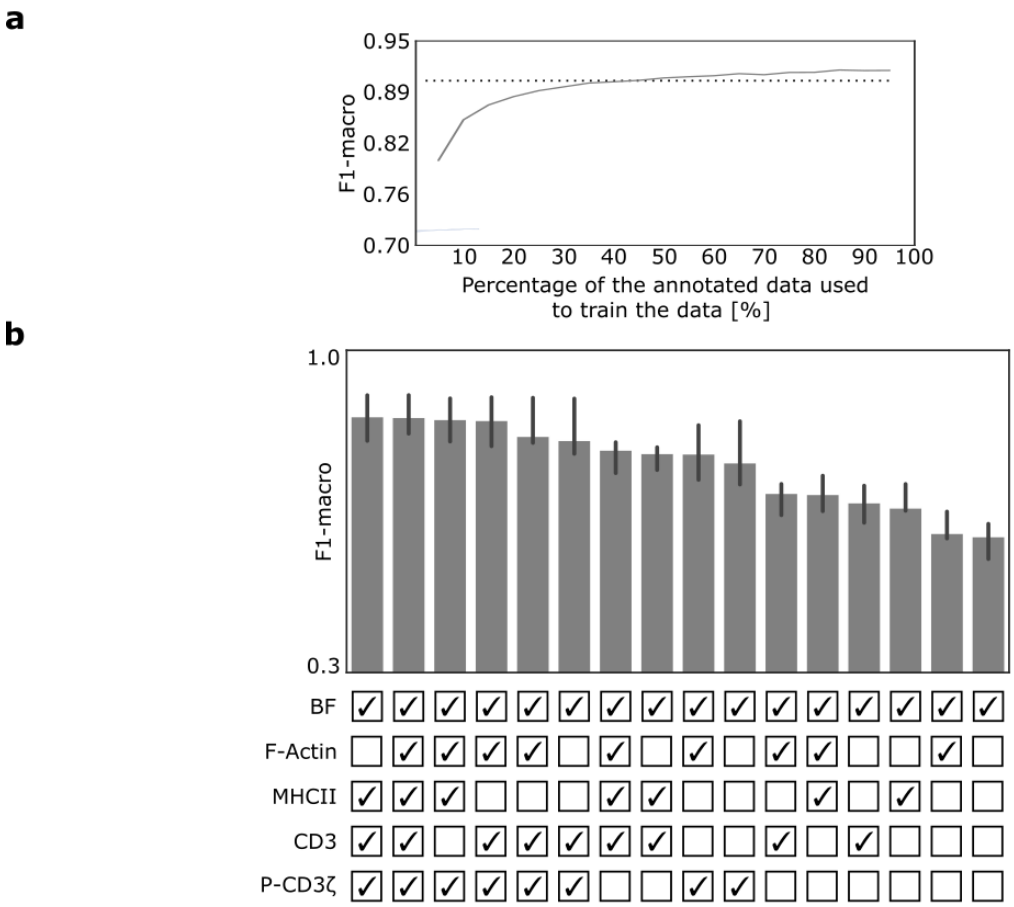

Supplementary Figure 5. Extracted information in the annotated data

a TSNE visualization of annotated images by only using the top features obtained in Fig1d.

b Number of annotated images vs. the classification performance

c The same XGBoost model was used to train the classifier. The training data was used for this evaluation using a 5-fold cross validation. In each step, features based on the selected channels were used for training the classifier. As brightfield (BF) is a stain-free channel, it is always kept in the data. The combinations are ranked based F1-macro.

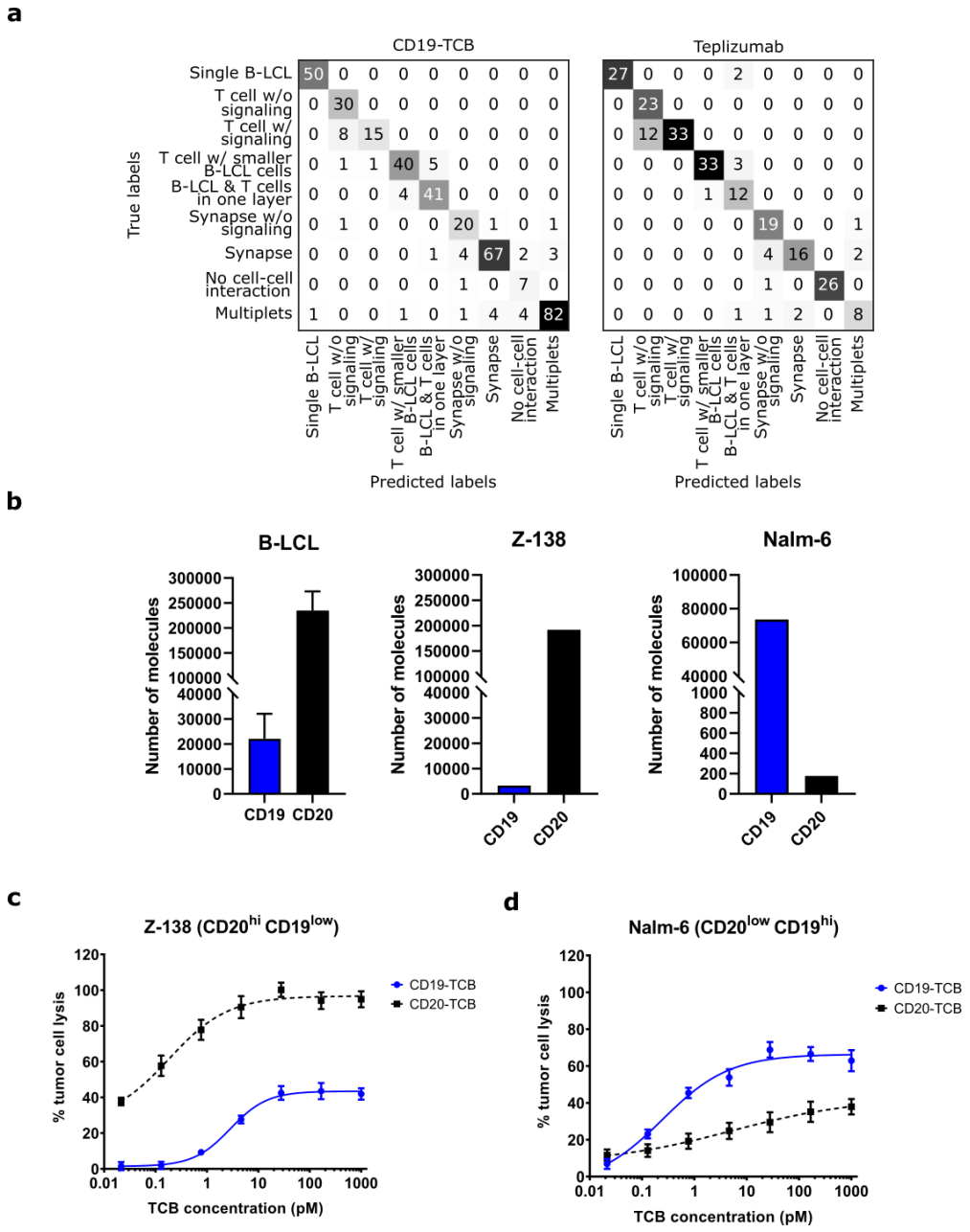

Supplementary Figure 6.

a Confusion matrix for classifications in CD19-TCB and Teplizumab based on 396 and 227 expert-annotated images, respectively. The previously trained model (Fig 1c) reached a macro F1-score of 0.86 and 0.85, respectively, on both datasets.

b Number of CD19 and CD20 molecules expressed on B-LCL, Nalm-6 and Z-138 cells. The measured values are derived from cell culture and were not measured in parallel to the experiment.

c,d Tumor cell lysis induced by CD19- and CD20-TCB, determined using LDH release after 24 h incubation of B-cell depleted human PBMCs with the tumor targets Nalm-6 or Z-138 and indicated TCB concentrations. One donor is shown.

Features	Category						
homogeneity_P-CD3zeta	texture	1	0	1	0	1	1
dissimilarity_P-CD3zeta	texture	-1	-1	-1	0	-1	-1
mean_intensity_ratio_P-CD3zeta_R5_R7	synaptic feature	1	0	1	1	1	1
mean_intensity_ratio_P-CD3zeta_R5_R6	synaptic feature	1	0	1	1	1	1
mean_intensity_ratio_CD3_R5_R7	synaptic feature	1	0	1	1	1	1
sum_intensity_ratio_CD3_R5_R7	synaptic feature	1	0	1	1	1	1
mean_intensity_ratio_CD3_R5_R6	synaptic feature	1	0	1	1	1	1
sum_intensity_ratio_CD3_R5_R6	synaptic feature	1	0	1	1	1	1
sum_intensity_ratio_MHCII_R5_R7	synaptic feature	1	0	1	1	1	1
sum_intensity_ratio_P-CD3zeta_R5_R7	synaptic feature	1	0	1	1	1	1
sum_intensity_ratio_P-CD3zeta_R5_R6	synaptic feature	1	0	1	1	1	1
mean_intensity_ratio_MHCII_R5_R6	synaptic feature	1	0	1	1	1	1
max_intensity_ratio_P-CD3zeta_R5_R6	synaptic feature	1	1	1	0	1	0
max_intensity_ratio_P-CD3zeta_R5_R7	synaptic feature	1	1	1	0	1	0
mean_intensity_ratio_MHCII_R5_R7	synaptic feature	1	0	1	1	1	1
sum_intensity_ratio_MHCII_R5_R6	synaptic feature	1	0	1	1	1	1
mask_based_eccentricity_P-CD3zeta	morphology	1	1	1	0	1	1
mask_based_eccentricity_CD3	morphology	1	1	1	0	1	1
mask_based_solidity_P-CD3zeta	morphology	-1	-1	-1	-1	-1	0
mask_based_solidity_MHCII	morphology	-1	-1	-1	-1	-1	0
mask_based_extent_P-CD3zeta	morphology	0	-1	-1	-1	-1	0
mask_based_extent_CD3	morphology	0	-1	-1	-1	-1	0
mask_based_extent_MHCII	morphology	-1	0	-1	-1	-1	0
mask_based_solidity_CD3	morphology	-1	-1	-1	-1	-1	0
sum_intensity_P-CD3zeta	intensity statistics	0	1	1	0	1	1
mean_intensity_P-CD3zeta	intensity statistics	1	1	1	1	1	1
skew_intensity_P-CD3zeta	intensity statistics	1	1	1	1	1	1
max_intensity_P-CD3zeta	intensity statistics	1	1	1	1	1	1
std_intensity_P-CD3zeta	intensity statistics	1	1	1	1	1	-1
kurtosis_intensity_P-CD3zeta	intensity statistics	1	1	1	1	1	1
shannon_entropy_P-CD3zeta	intensity statistics	1	1	1	1	1	-1
dice_distance_MHCII_P-CD3zeta	colocalization	-1	0	-1	-1	-1	-1
correlation_distance_R6_CD3_R7_P-CD3zeta	colocalization	-1	-1	-1	-1	-1	-1
correlation_distance_R4_F-Actin_R5_MHCII	colocalization	-1	-1	0	0	-1	-1
euclidean_distance_R7_P-CD3zeta_R6_CD3	colocalization	-1	-1	0	-1	0	-1
euclidean_distance_R6_CD3_R7_P-CD3zeta	colocalization	-1	-1	0	-1	0	-1
correlation_distance_R7_P-CD3zeta_R6_CD3	colocalization	-1	-1	-1	-1	-1	-1
jaccard_distance_MHCII_P-CD3zeta	colocalization	-1	0	-1	-1	-1	-1
correlation_distance_R6_CD3_R5_MHCII	colocalization	-1	0	-1	-1	-1	-1
correlation_distance_R5_MHCII_R6_CD3	colocalization	-1	0	-1	-1	-1	-1
jaccard_distance_MHCII_CD3	colocalization	-1	0	-1	-1	-1	-1
dice_distance_MHCII_CD3	colocalization	-1	0	-1	-1	-1	-1
correlation_distance_R7_P-CD3zeta_R5_MHCII	colocalization	-1	0	-1	-1	-1	-1
correlation_distance_R5_MHCII_R7_P-CD3zeta	colocalization	-1	0	-1	-1	-1	-1
correlation_distance_R5_MHCII_R4_F-Actin	colocalization	-1	-1	0	0	-1	-1

Supplementary Table 1. Significant features induced by CD19-TCB

The table represents the features that significantly changed for at least four donors due to stimulation by CD19-TCB. The table represents the list of consistent features from Fig. 3a. 1 represents a significant increase (red in Fig. 3a), -1 represents a significant decrease (blue in Fig. 3a) and 0 represents no significant change (gray in Fig. 3a).

Features	Category							
homogeneity_F-Actin	texture	-1	-1	1	-1	-1	-1	1
energy_F-Actin	texture	-1	0	1	-1	-1	-1	1
ASM_F-Actin	texture	-1	0	1	-1	-1	-1	1
energy_P-CD3zeta	texture	0	-1	-1	-1	1	1	-1
ASM_P-CD3zeta	texture	0	-1	-1	-1	1	1	-1
max_intensity_ratio_P-CD3zeta_R5_R7	synaptic feature	-1	-1	0	-1	-1	-1	0
sum_intensity_F-Actin	intensity statistics	-1	-1	1	-1	-1	-1	1
min_intensity_P-CD3zeta	intensity statistics	1	1	-1	1	0	1	0
sum_intensity_P-CD3zeta	intensity statistics	1	0	-1	1	0	1	1
skew_intensity_P-CD3zeta	intensity statistics	0	0	-1	-1	-1	0	-1
shannon_entropy_F-Actin	intensity statistics	-1	-1	1	-1	-1	-1	1
max_intensity_F-Actin	intensity statistics	-1	-1	1	-1	-1	-1	1
min_intensity_F-Actin	intensity statistics	-1	-1	1	-1	-1	-1	1
std_intensity_F-Actin	intensity statistics	-1	-1	1	-1	-1	-1	1
mean_intensity_F-Actin	intensity statistics	-1	-1	1	-1	-1	-1	1
euclidean_distance_R7_P-CD3zeta_R4_F-Actin	colocalization	-1	-1	1	-1	-1	-1	1
euclidean_distance_R4_F-Actin_R7_P-CD3zeta	colocalization	-1	-1	1	-1	-1	-1	1
manders_overlap_coefficient_R5_MHCII_R4_F-Actin	colocalization	1	1	-1	-1	1	1	-1
manders_overlap_coefficient_R7_P-CD3zeta_R4_F-Actin	colocalization	1	1	-1	1	1	1	-1
manders_overlap_coefficient_R4_F-Actin_R7_P-CD3zeta	colocalization	1	1	-1	1	1	1	-1
structural_similarity_R5_MHCII_R7_P-CD3zeta	colocalization	-1	-1	1	0	-1	-1	1
structural_similarity_R7_P-CD3zeta_R5_MHCII	colocalization	-1	-1	1	0	-1	-1	1
manders_overlap_coefficient_R4_F-Actin_R5_MHCII	colocalization	1	1	-1	-1	1	1	-1

Supplementary Table 2. Significant features induced by Teplizumab

The table represents the features that significantly changed for at least six donors due to stimulation by Teplizumab. The table represents the list of consistent features from Fig. 3h. 1 represents a significant increase (red in Fig. 3h), -1 represents a significant decrease (blue in Fig. 3h) and 0 represents no significant change (gray in Fig. 3h).